Report

Title: Attention samples features rhythmically

Authors: Daniele Re[1]*, Maya Inbar[2]* Craig G. Richter[3] and Ayelet N. Landau[1]§

Affiliation:

[1] Departments of Psychology and of Cognitive Science, the Hebrew University of Jerusalem, Jerusalem, Mt. Scopus, 91905, Israel

[2] Department of Linguistics, the Hebrew University of Jerusalem, Mt. Scopus, Jerusalem, 91905, Israel

[3] Basque Center on Cognition, Brain and Language (BCBL), Mikeletegi Pasealekua 69, 20009, Donostia, Spain

* These authors contributed equally

§Lead Contact and Corresponding author: ayelet.landau@mail.huji.ac.il

Summary

Attention supports the allocation of resources to relevant locations and objects in a scene. Under most conditions, several stimuli compete for neural representation. Attention biases neural representation toward the response associated with the attended object [1, 2]. Therefore, an attended stimulus enjoys a neural response that resembles the response to that stimulus in isolation. Factors that determine and generate attentional bias have been researched, ranging from endogenously controlled processes to exogenous capture of attention [1–4]. Recent studies investigate the temporal structure governing attention. When participants monitor a single location, visual-target detection depends on the phase of an ~8 Hz brain rhythm [5, 6]. When two locations are monitored, performance fluctuates at 4 Hz for each location [7, 8]. The hypothesis is that 4 Hz sampling for two locations may reflect a common sampler that operates at 8 Hz globally which is divided between relevant locations [5–7, 9]. The present study targets two properties of this phenomenon, called rhythmic-attentional sampling: First, sampling is typically described for selection over different locations. We examined whether rhythmic sampling is limited to selection over space or whether it extends to feature-based attention. Second, we examined whether sampling at 4 Hz results from the division of an 8 Hz rhythm over two objects. We found that two overlapping objects defined by features are sampled at ~4 Hz per object. In addition, performance on a single object fluctuated at 8 Hz. Rhythmic sampling of features did not result from temporal structure in eye movements.

Results

When two locations compete for resources, ongoing performance fluctuates at 4 Hz per location, in alternation. Several studies have replicated and expanded the basic findings of rhythmic sampling [10–15]. In addition, a physiological signature – the visual-gamma-band-response – tracks rhythmic sampling when attention is distributed across visual hemifields [16]. Recent work in awake behaving animals suggests that interactions between adjacent receptive fields generate rhythmic multi-unit activity (MUA) which is consistent with rhythmic sampling [17]. The multi-unit finding provides a putative generative mechanism for rhythmic sampling. Other studies have reported the engagement of frontoparietal attentional-control regions in the generation of rhythmic sampling [18, 19].

To date, all descriptions of rhythmic sampling in vision examined sampling of different locations. Features, which are non-spatial properties of objects, can also cue attentional selection; such selection processes are called feature-based attention. Here, we investigate whether rhythmic sampling extends beyond the case of spatial selection. Understanding the scope of rhythmic sampling bears consequences on the type of mechanisms that may account for it. If rhythmic sampling is a phenomenon limited to spatial attention, its mechanisms may rely on the spatial architecture of the visual system. If rhythmic sampling extends beyond spatial attention, this may point to a more general account for this phenomenon both within and beyond the visual system.

Rhythmic sampling beyond spatial attention

We examined performance in a task that required ongoing distributed attention over two objects superimposed in space (Figure 1A). Stimuli were two clouds of moving

dots [20] that appeared at the same location but were easily distinguishable. Each cloud was defined by a different dot motion direction and color. The onsets of the respective clouds were asynchronous (onset asynchrony, Δ = 0.2-0.73 s). Stimulus presentation lasted up to 2.25 s. Participants were instructed to report a brief color change (30 ms) that occurred within one of the two superimposed clouds. The brief change affected 50% of the cloud-dots, and had one of eight target intensities. The color change could appear in one of 26 time bins following the second cloud onset (ranging from Δ+0.25 to Δ+0.75 s; exhaustively spaced with respect to the second cloud onset). The asynchronous onsets, and specifically the onset of the second cloud, contributed to the individuation of the two clouds, but also served as a *reset*. The assumption is that the onset of a new cloud captures attention [21]. Thus, including this reset in the design generates a reproducible attentional dynamic over multiple trials. The combination of exhaustive target spacing and the reset event allows the measurement of temporal structure in ongoing behavioral performance [7]. Finally, although rhythmic sampling was previously assessed by measuring accuracy at a pre-defined target intensity, we included several target intensities within the main experiment, and selected the intensity closest to threshold performance during offline analysis (Figure 2A, Figure S4A).

We found that feature selection proceeded rhythmically. Performance on the two clouds fluctuated at ~4 Hz per cloud. As can be seen in Figure 3A, the spectra for both first and second cloud performance revealed significant peaks at 4 Hz ($p = 0.019$ and $p = 0.0003$ for first and second cloud respectively, multiple comparisons corrected). An analysis of the phase relation between the 4 Hz performance fluctuations of each cloud revealed that the phases were not significantly different from a uniform distribution (Figure 3B; Rayleigh test for non-uniformity, $p = 0.81$). Analyzing

performance for a target-intensity which results in an average performance of 50% ensures that performance over time can be maximally modulated and thus could reveal temporal structure in ongoing performance. Nonetheless, an additional analysis that pooled data with accuracy levels ranging from 25% to 75% demonstrates the same result robustly ($p < 0.001$). Finally, analyzing different accuracy levels separately within this range also reveals the same pattern of results.

Our findings demonstrate that rhythmic sampling occurs not only for the case of spatial selection, but also governs selection among superimposed items defined by features. An analysis of the phase relations of performance on the first and second cloud revealed that different participants had different phase relations, indicating that as opposed to rhythmic sampling over locations, the relation of performance on one object was not consistently in opposition to the performance on the other object.

Controlling for eye movements

Recently, several groups have investigated the link between saccade generation and fluctuations in performance and brain activity [14, 22–26]. For example, Bellet et al. [23] reveals rhythmicity in performance as a function of saccade onset when attention is distributed over two locations. In the present study, attention is not distributed over multiple locations; therefore, the reported spatial patterns of microsaccades during spatial selection and their underlying processes do not apply to our experimental design.

However, moving stimuli often generate microsaccades (MSs) in a consistent direction relative to movement [27], a pattern which may itself be related to performance fluctuations. An examination of the eye position in our data reveals that such directional selectivity of MSs is also present in response to our stimuli (Figure

S3). Importantly, however, MS execution during stimulus presentation in the present study is sparse. We repeated the analysis of accuracy performance using MS-free trials only. This analysis revealed the same pattern of results as the inclusion of all trials (see Figure S2A-C and STAR methods). Thus, fluctuations in performance cannot readily be the consequence of either MS-rate fluctuations or temporal structure present in MS direction [25].

Evidence for common sampling at 8 Hz

Previously, 4 Hz rhythmic sampling was assumed to reflect a common sampler operating at 8 Hz [7, 28]. Such a sampler may be intrinsic to the selection process or could be a global, non-selective, drive that governs local interactions within the sensory substrate [29–31]. Regardless of the specific implementation, the common sampler account assumes that rhythmic sampling at 4 Hz for two objects is the result of dividing 8 samples over two relevant items. Studies documenting 8 Hz "perceptual cycles" measure perception as a function of oscillatory brain activity [9, 32–35] and utilize vastly different experimental setups and attentional control as compared to those measuring rhythmic sampling. This results in task demands and analytic approaches that have so far only suggestively linked the 8 Hz of "perceptual cycles" with the 4 Hz of "attentional sampling". We sought to examine this putative link using identical stimuli and experimental demands.

In a second experiment, participants were presented with a single moving dot-cloud, rather than two separate clouds. We used the same color-change target presented at 26 time bins relative to the stimulus onset (Figure 1B).

If rhythmic sampling at 4 Hz indeed results from the division of a common 8 Hz sampler, an 8 Hz fluctuation should be measured in the single-cloud experiment.

Conversely, if rhythmic sampling is a separate phenomenon from the 8 Hz modulation previously described as a function of EEG phase [5, 6], then behavioral performance on a single cloud may not fluctuate at all. Such a finding would indicate that rhythmic sampling may be a mechanism dedicated to resolving interactions among competing stimuli when several items are task relevant.

We found that performance on a single cloud proceeded rhythmically at double the frequency of the two-cloud sampling – 8 Hz (Figure 3C; $p = 0.04$ for the accuracy analysis, multiple comparisons corrected). There was no significant peak at any other frequency in the spectrum. This finding is consistent with previously documented fluctuations in performance as a function of rhythmic brain activity at a similar rhythm [5, 6, 9]. An additional analysis that pooled data with accuracy levels ranging from 25% to 75% demonstrated the same result robustly ($p<0.001$). Together, the two experiments demonstrate with near identical stimuli and task demands that selection of one cloud proceeds at 8 Hz and that when two clouds are presented in superposition, the rhythmic sampling results in a 4 Hz performance pattern in each cloud.

The single-cloud experiment also included a large proportion of trials with no MSs. An analysis including MS-free trials only revealed the exact same pattern of results as the inclusion of all trials (Figure S2D, E). Thus, the 8 Hz fluctuations in performance cannot be the consequence of either MS-rate fluctuations or temporal structure present in MS direction [25].

The present experimental design allowed for measurement of both accuracy and threshold fluctuation in performance (see STAR methods). Before discussing the implications of our main results we briefly note the merits and pitfalls of this new

experimental procedure. At a technical level, including several target-intensities in the main experiment is in place of an independent estimation of perceptual thresholds (as previously required). The multitude of target intensities generates data for offline calculation of perceptual thresholds. Additionally, the inclusion of several target-intensities allows for the investigation of performance fluctuations for different accuracy levels, and importantly, fluctuations in threshold-intensity performance – a more continuous measure of perceptual sensitivity as a function of time. Threshold fluctuations show similar spectral patterns as the accuracy measures (Figure 4). However, all things considered, we would like to note that accuracy performance provided a more robust and stable finding of rhythmic sampling in both experiments.

Discussion

The present study reveals rhythmic sampling beyond spatial attention – selection processes that are cued by non-spatial features proceed rhythmically. Two dot-motion clouds were superimposed in space and defined by non-spatial properties: motion direction, dot color as well as an asynchrony in the onsets of the two clouds. By design, participants were able to readily identify the two clouds, and performance fluctuated rhythmically at 4 Hz for targets in each of them.

In addition, we also demonstrate frequency doubling when comparing performance on two objects to performance on a single object. Ongoing performance on two clouds proceeded at ~4 Hz per cloud while ongoing performance on one cloud proceeded at 8 Hz. This provides the "missing link" between the phenomenon of "perceptual cycles" previously documented with non-invasive physiology (EEG) [6] and rhythmic-attentional sampling [7, 31], documented in behavioral experiments. This is

suggestive that indeed ~8 Hz fluctuations form the basic period with which we explore our environment and that this common drive is the determining factor of the rhythmic sampling measured at ~4 Hz.

Feature-based attention shares several properties with spatial attention. For example, both forms of selection have a similar effect on the response magnitude and correlation structure of neuronal populations [36, 37]. There are, however, important differences between feature-based, and spatial attention. The modulation of neural responses to a selected feature (e.g., color or motion direction) tends to affect neural populations that respond beyond the spatial scope of attended stimuli, and could even extend to the hemisphere processing unattended stimuli [36, 38, 39]. Thus, the implementation of feature-based attention is not specific to the location of the object bearing the selected feature – it is global. Here, we document that the implementation of feature-based attention, like spatial attention, is rhythmic. Contrary to rhythmic sampling over space, however, the relation of the 4 Hz sampling of the first and second cloud is not fixed in anti-phase as shown for spatial attention, but rather variable in the group of individuals tested here. Rephrased, our experimental design generated inter-individual heterogeneity in the temporal relations of performance on the two clouds. Future studies will determine whether this heterogeneity is indeed a defining property of feature attention or whether it results from suboptimal estimation of phase relations, in spite of the robust finding of a 4 Hz peak in performance accuracy for both clouds.

How do these findings qualify our understanding of the mechanisms generating and governing rhythmic sampling? The field is far from agreement on the

neurophysiology of rhythmic sampling. In what follows we discuss our findings in the context of different accounts that have recently been proposed.

According to one account, rhythmicity could be a generic, reflexive property of the neural substrate. Accordingly, the sampling dynamic results from local interactions between the response-strength of different neuronal populations. Thus, two objects – a red and a blue cloud – could engage in mutual inhibition that results in the successful representation of one of the two objects at any given cycle of a global rhythmic drive. For example, alpha oscillations (~8-12 Hz), which are readily measured over visual areas using non-invasive physiology, are considered a rhythmic-inhibitory drive, globally present in the visual cortex [34, 35, 40–42]. It is possible that this type of global rhythmic temporal structure at ~8 Hz shapes ongoing perception and, together with inhibitory interactions of competing objects [1], results in the division of the rhythmic sampling from 8 Hz to 4 Hz [29, 31]. This logic fits well with findings in spatial attention, where the phase relation between performance in one location and performance in another location are in perfect alternation. Here, we did not find anti-phase relations for the 4 Hz fluctuations in performance on one vs. the other cloud – but rather the phase relations were uniformly distributed as discussed above.

Another account [18], is that rhythmic sampling is inherent to mechanisms controlling attention. Several networks and brain structures have been proposed for generating such control signals onto the sensory substrate [21, 43, 44]. Specifically, Fiebelkorn et al. [18, 45] have demonstrated that frontoparietal networks account for rhythmic fluctuations in performance. Attributing sampling to this substrate is, in essence, attributing this rhythmic mechanism to attentional control regions as opposed to local interactions within the sensory substrate.

Finally, a recent study documented that center-surround receptive field interactions generate rhythmic neuronal activity that matched fluctuations in detection performance of awake behaving non-human primates [17]. Accounting for rhythmic sampling with center-surround interactions is suggestive of a reflexive mechanism that is inherent to the spatial architecture of the visual system – i.e., the classical receptive fields. It remains to be shown whether such local interactions capture the entire scope of rhythmic sampling. For example, rhythmic sampling was described over distant parts of the visual field – and commonly between the two visual hemi-fields [7, 8, 14, 16].

Our finding that feature-based attention proceeds rhythmically further supports an implementation of rhythmic sampling that is not limited to spatial-receptive-field interactions. Rhythmic sampling in feature-based attention, as well as the direct demonstration of sampling-frequency doubling – when two clouds become one – suggest that rhythmic sampling is a general rhythmic mechanism that shapes ongoing performance as well as serves to structure selection processes in light of competition.

Acknowledgments

This work was supported by funds from the James McDonnell Scholar Award for Understanding Human Cognition as well as the National Israeli Psychobiology Institute (both awarded to ANL). MI is supported by the Humanities Fund PhD program in Linguistics and the Jack, Joseph and Morton Mandel School for Advanced Studies in the Humanities, and CGR via the Spanish Ministry of Economy and Competitiveness, through the "Severo Ochoa" Programme for Centres/Units of Excellence in R&D" (SEV-2015-490). The authors would like to thank Dr. Flor Kusnir, Shany Grossman and Yaniv Abir, Elio Balestrieri, and other members of the brain attention and time lab (www.landaulab.com) for insightful comments on the work.

Author Contributions

Conceptualization, D.R. and A.N.L.; Methodology, D.R. and A.N.L.; Software, D.R.; Formal Analysis, D.R. and M.I.; Investigation, D.R.; Visualization, D. R., A.N.L., M.I.; Writing – Original Draft, D.R. and A.N.L.; Writing -- Review & Editing, D.R., M.I., C.G.R. and A.N.L.; Supervision, A.N.L.; Funding Acquisition, A.N.L.

Declaration of Interests

The authors declare no competing interests.

References

1. Reynolds, J. H., Chelazzi, L., and Desimone, R. (1999). Competitive mechanisms subserve attention in macaque areas V2 and V4. J. Neurosci. *19*, 1736–1753.

2. Beck, D. M., and Kastner, S. (2009). Top-down and bottom-up mechanisms in biasing competition in the human brain. Vision Res. *49*, 1154–1165.

3. Landau, A. N., Esterman, M., Robertson, L. C., Bentin, S., and Prinzmetal, W. (2007). Different effects of voluntary and involuntary attention on EEG activity in the gamma band. J. Neurosci. *27*, 11986–11990.

4. Buschman, T. J., and Miller, E. K. (2009). Serial, Covert Shifts of Attention during Visual Search Are Reflected by the Frontal Eye Fields and Correlated with Population Oscillations. Neuron *63*, 386–396.

5. Busch, N. A., Dubois, J., and VanRullen, R. (2009). The phase of ongoing EEG oscillations predicts visual perception. J. Neurosci. *29*, 7869–7876.

6. VanRullen, R. (2016). Perceptual Cycles. Trends Cogn. Sci. *0*, 174–205.

7. Landau, A. N., and Fries, P. (2012). Attention samples stimuli rhythmically. Curr. Biol. *22*, 1000–1004.

8. Fiebelkorn, I. C., Saalmann, Y. B., and Kastner, S. (2013). Rhythmic sampling within and between objects despite sustained attention at a cued location. Curr. Biol. *23*, 2553–2558.

9. Mathewson, K. E., Gratton, G., Fabiani, M., Beck, D. M., and Ro, T. (2009).

To see or not to see: prestimulus phase predicts visual awareness. J. Neurosci. *29*, 2725–2732.

10. Tomassini, A., Ambrogioni, L., Medendorp, W. P., and Maris, E. (2017). Theta oscillations locked to intended actions rhythmically modulate perception. Elife *6*, 1–18.

11. Song, K., Meng, M., Chen, L., Zhou, K., and Luo, H. (2014). Behavioral oscillations in Attention: rhythmic alpha pulses mediated through theta band. J. Neurosci. *34*, 4837–4844.

12. Ho, H. T., Leung, J., Burr, D. C., Alais, D., and Morrone, M. C. (2017). Auditory sensitivity and decision criteria oscillate at different frequencies separately for the two ears. Curr. Biol., 1–7.

13. Benedetto, A., Spinelli, D., Morrone, M. C., Spaak, E., Lange, F. de, Jensen, O., Tomassini, A., Spinelli, D., Jacono, M., Sandini, G., et al. (2016). Rhythmic modulation of visual contrast discrimination triggered by action. Proc. Biol. Sci. *283*, 3536–3544.

14. Hogendoorn, H. (2016). Voluntary saccadic eye movements ride the attentional rhythm. J. Cogn. Neurosci. *28*, 1625–1635.

15. Dugué, L., Roberts, M., and Carrasco, M. (2016). Attention Reorients Periodically. Curr. Biol. *26*, 1595–1601.

16. Landau, A. N., Schreyer, H. M., Van Pelt, S., and Fries, P. (2015). Distributed Attention Is Implemented through Theta-Rhythmic Gamma Modulation. Curr. Biol. *25*, 2332–2337.

17. Kienitz, R., Schmiedt, J. T., Shapcott, K. A., Kouroupaki, K., Saunders, R. C., and Schmid, M. C. (2018). Theta Rhythmic Neuronal Activity and Reaction Times Arising from Cortical Receptive Field Interactions during Distributed Attention. Curr. Biol. *28*, 2377–2387.e5.

18. Fiebelkorn, I. C., Pinsk, M. A., and Kastner, S. (2018). A Dynamic Interplay within the Frontoparietal Network Underlies Rhythmic Spatial Attention. Neuron *99*, 842–853.e8.

19. Helfrich, R. F. (2018). The rhythmic nature of visual perception. J. Neurophysiol. *119*, 1251–1253.

20. Braddick, O. (1974). A short-range process in apparent motion. Vision Res. *14*, 519–527.

21. Nobre, A. C. (2018). Attention. In Stevens' Handbook of Experimental Psychology and Cognitive Neuroscience, Sensation, Perception, and Attention, J. Wixted and J. Serences, eds. (John Wiley & Sons, Inc. New York), p. 241.

22. Hafed, Z. M. (2013). Alteration of Visual Perception prior to Microsaccades. Neuron *77*, 775–786.

23. Bellet, J., Chen, C.-Y., and Hafed, Z. M. (2017). Sequential hemifield gating of alpha and beta behavioral performance oscillations after microsaccades. J. Neurophysiol., jn.00253.2017.

24. Staudigl, T., Hartl, E., Noachtar, S., Doeller, C. F., and Jensen, O. (2017). Saccades are phase-locked to alpha oscillations in the occipital and medial temporal lobe during successful memory encoding. PLOS Biol. *15*, e2003404.

25. Bosman, C. A., Womelsdorf, T., Desimone, R., and Fries, P. (2009). A microsaccadic rhythm modulates gamma-band synchronization and behavior. J. Neurosci. *29*, 9471–9480.

26. Benedetto, A., and Morrone, M. C. (2017). Saccadic Suppression Is Embedded Within Extended Oscillatory Modulation of Sensitivity. J. Neurosci. *37*, 3661–3670.

27. Pola, J., Wyatt, H. J., and Lustgarten, M. (1995). Visual fixation of a target and suppression of optokinetic nystagmus: Effects of varying target feedback. Vision Res. *35*, 1079–1087.

28. VanRullen, R., Carlson, T., and Cavanagh, P. (2007). The blinking spotlight of attention. Proc. Natl. Acad. Sci. U. S. A. *104*, 19204–19209.

29. Jensen, O., Gips, B., Bergmann, T. O., and Bonnefond, M. (2014). Temporal coding organized by coupled alpha and gamma oscillations prioritize visual processing. Trends Neurosci. *37*, 357–369.

30. Klimesch, W., Sauseng, P., and Hanslmayr, S. (2007). EEG alpha oscillations: The inhibition–timing hypothesis. Brain Res. Rev. *53*, 63–88.

31. Landau, A. N. (2018). Neuroscience: a neural mechanism for rhythmic sampling. Curr. Biol., 830–832.

32. Busch, N. A., Dubois, J., and VanRullen, R. (2009). The phase of ongoing {EEG} oscillations predicts visual perception. J. Neurosci. *29*.

33. Hanslmayr, S., Volberg, G., Wimber, M., Dalal, S. S., and Greenlee, M. W. (2013). Prestimulus oscillatory phase at 7 Hz gates cortical information flow

and visual perception. Curr. Biol. *23*, 2273–2278.

34. Romei, V., Brodbeck, V., Michel, C., Amedi, A., Pascual-Leone, A., and Thut, G. (2007). Spontaneous Fluctuations in Posterior alpha-Band EEG Activity Reflect Variability in Excitability of Human Visual Areas. Cereb. Cortex *18*, 2010–2018.

35. Thut, G., and Miniussi, C. (2009). New insights into rhythmic brain activity from TMS–EEG studies. Trends Cogn. Sci. *13*, 182–189.

36. Cohen, M. R., and Maunsell, J. H. R. (2011). Using Neuronal Populations to Study the Mechanisms Underlying Spatial and Feature Attention. Neuron *70*, 1192–1204.

37. Treue, S. (2014). The Oxford Handbook of Attention A. C. (Kia) Nobre and S. Kastner, eds. (Oxford University Press).

38. Serences, J. T., and Boynton, G. M. (2007). Feature-Based Attentional Modulations in the Absence of Direct Visual Stimulation. Neuron *55*, 301–312.

39. Maunsell, J. H. R., and Treue, S. (2006). Feature-based attention in visual cortex. Trends Neurosci. *29*, 317–322.

40. Berger, H. (1930). Uber das Elektrenkephalogramm des Menschen. Zweite Mitteilung. J. Psycho. Neurol. *40*, 160–179.

41. Haegens, S., Händel, B. F., and Jensen, O. (2011). Top-down controlled alpha band activity in somatosensory areas determines behavioral performance in a discrimination task. J. Neurosci. *31*, 5197–5204.

42. Spaak, E., Bonnefond, M., Maier, A., Leopold, D. A., and Jensen, O. (2012). Layer-Specific Entrainment of Gamma-Band Neural Activity by the Alpha Rhythm in Monkey Visual Cortex. Curr. Biol. *22*, 2313–2318.

43. Buschman, T. J., and Kastner, S. (2015). From Behavior to Neural Dynamics: An Integrated Theory of Attention. Neuron *88*, 127–144.

44. Bressler, S. L., Tang, W., Sylvester, C. M., Shulman, G. L., and Corbetta, M. (2008). Top-Down Control of Human Visual Cortex by Frontal and Parietal Cortex in Anticipatory Visual Spatial Attention. J. Neurosci. *28*, 10056–10061.

45. Helfrich, R. F., Fiebelkorn, I. C., Szczepanski, S. M., Lin, J. J., Parvizi, J., Knight, R. T., and Kastner, S. (2018). Neural Mechanisms of Sustained Attention Are Rhythmic. Neuron *99*, 854–865.e5.

46. Peirce, J. W. (2007). PsychoPy-Psychophysics software in Python. J. Neurosci. Methods *162*, 8–13.

47. Oostenveld, R., Fries, P., Maris, E., and Schoffelen, J.-M. (2011). FieldTrip: Open Source Software for Advanced Analysis of MEG, EEG, and Invasive Electrophysiological Data. Comput. Intell. Neurosci. *2011*, 1–9.

48. Prins, N., and Kingdom, F. A. A. (2009). Palamedes: Matlab routines for analyzing psychophysical data. http://www.palamedestoolbox.org.

49. Harris, J. (1978). On then Use of Windows with the Discrete for Harmonic Analysis Fourier Transform. Proc. IEEE *66*, 51–83.

50. Amit, R., Abeles, D., Bar-Gad, I., and Yuval-Greenberg, S. (2017). Temporal dynamics of saccades explained by a self-paced process. Sci. Rep. *7*, 886.

51. Engbert, R., and Kliegl, R. (2003). Microsaccades uncover the orientation of covert attention. Vision Res. *43*, 1035–1045.

52. Berens, P. (2009). CircStat: a MATLAB toolbox for circular statistics. J. Stat. Softw. *31*, 1–21.

Figure Captions

Figure 1: Stimuli and task procedure. Dot-motion clouds were used for both experiments. The detection target was a decrement in saturation that affected 50% of the elements of a given cloud stimulus. Participants were instructed to press a button if they detected a target. (A) The two-cloud experiment consisted of two superimposed dot-motion clouds that were defined by motion direction and color. The first cloud preceded the second cloud with a variable interval Δ (0.2-0.73 s). Target occurrence was exhaustive, i.e. at all possible onset points, relative to the second-cloud onset and could occur within either cloud. The magnified timeline and vertical bars signify possible target times over the course of an experiment. A given trial never had more than one target. (B) The single-cloud experiment consisted of one dot-motion cloud. Targets were presented exhaustively relative to cloud onset. See also Figure S1

Figure 2: Time course of detection accuracy (A, C) and intensity thresholds (B, D) for the two-cloud and single cloud experiments (A, B and C, D, respectively). Note that time average data only loosely represents the results reported here, since the main findings are generated from single-subject spectral analysis which is then entered into the statistical model or averaged for display purposes. Shaded regions denote ±SEM. See also Figure S2 and Figure S4.

Figure 3: Spectral analysis results of accuracy time courses from the two-cloud and single-cloud experiments. (A, C) Amplitude spectra for the two-cloud and one-cloud experiments. Blue and red lines represent first and second cloud stimuli. (B) Phase histograms for the phase relation between the first and second object accuracy performance at 4 Hz. Significance in all spectra, corrected for multiple comparisons ($p<0.05$), is denoted by a horizontal line above the significant frequency peaks. Shaded regions denote ±SEM. See also Figure S2.

Figure 4: Threshold-intensity spectral analysis results from the (A) two-cloud and (B) single-cloud experiments. Shaded regions denote ±SEM.

STAR Methods

Contact for reagent and resource sharing

Further information and requests for resources should be directed to and will be fulfilled by the Lead Contact, Ayelet N. Landau (ayelet.landau@mail.huji.ac.il).

Experimental model and subject details

Twenty-five individuals (16 females, 3 left handed, average age 25) with normal or corrected-to normal visual acuity participated in the two-item experiment, and thirty-six individuals (19 females, 7 left handed, average age 24) with normal or corrected-to normal visual acuity participated in the one-cloud experiment. Participants gave informed consent before the experimental session and received monetary compensation. The study was approved by the institutional review board of ethical conduct at the Hebrew University of Jerusalem.

Method details

Apparatus and stimuli

The stimuli and experimental software were generated using python (PsychoPy2 toolbox [46], python version: 2.7.11). Stimuli were presented on a BenQ XL2420Z LCD screen with 100 Hz refresh rate, 1920 x 1080 resolution, positioned 57 cm from the participant. During both experiments, participants were instructed to gaze centrally at a grey cross (0.9° visual angle; RGB value: [0.7;0.7;0.7]) during the entire trial. The stimulus consisted of a dot-motion cloud with 400 randomly scattered dots moving coherently (100% coherence) across a 3° circular aperture with a grey background. Dots lasted as long as they were visible within the annular borders of the clouds (i.e., dot life-time infinite), and had a speed of 0.86 deg/s. Initial cloud luminance values for the blue and red clouds were 20 and 52 cd/m^2 respectively. Colors were set on a HSV space and the detection-target was a brief (30 ms) decrease in saturation of 200 randomly selected dots, out of the 400 dots making up a cloud. The decrement in saturation had 8 different levels (i.e., target intensities) tailored for each participant following a short training. The training included performing on trials with 10 different levels of color-saturation decrements for each cloud (red and blue) separately. The saturation-decrement levels ranged from 0.5 – 1 (HSV) on a gamma corrected monitor, each repeating twice. For the main experiment a subset of 8 saturation-decrement values was selected based on performance in the training block and each intensity level was repeated 5 times per time bin. Saturation-decrement values were selected based on training. Floor and ceiling values were identified within the 10 levels presented in training, these values formed a range that was then divided into 8 equally-spaced saturation-decrement levels, referred to as

target-intensity levels in the manuscript. Ten percent of the trials did not include a target (i.e., catch trials). False alarms were rare and were below 1% on average (0.75% and 0.5% for the two- and one-cloud experiment respectively). The two-cloud experiment included a total of 2288 trials ran over two sessions and the single-cloud experiment included a total of 1144 trials ran within a single session.

For both experiments, the fixation cross was present on the screen throughout the trial. Each trial started with a variable fixation period of 0.5-0.8 s followed by a stimulus onset. During both experiments eye movements were monitored using a high-speed infrared eye tracking camera (Eyelink 1000, SR Research). Blinks or saccades exceeding 2° visual angle radius away from fixation were marked as fixation violations, resulting in exclusion of the trial. Excluded trials were repeated to ensure the acquisition of full data sets for all participants at the end of each experimental block.

Design and procedure

Two-cloud experiment

The two-cloud experiment began with a familiarization stage that lasted approximately 15 minutes. During the familiarization stage, participants performed target detection on single-cloud stimuli. The single-cloud stimuli were used in training in order to promote the individuation of the different clouds as well as in order to familiarize the participants with the experimental setup and task. In the main experiment, following the fixation period, a blue cloud was presented centrally for up to 2.25 s after stimulus onset. Following a variable time between 0.2-0.73 s (denoted Δ), a red cloud was added to the display with an orthogonal motion direction. The target could appear after the second cloud onset at one of 26 possible times ranging Δ+0.25 to Δ +0.75 seconds; i.e., exhaustive relative to the second cloud onset. Accuracy was calculated based on RT distribution. A response was labeled corrected if reaction times were delivered within 1.5 s after target onset. In addition, reaction times shorter than 100 ms or longer than two standard deviations above the mean were discarded as likely resulting from an erroneous response (means and standard deviations were calculated separately per target color and per saturation level). For both experiments in the absence of target-detection or during catch trials, no response was required and the stimulus terminated after 2.25 s followed by the next trial.

Single-cloud experiment

After the fixation period, a blue dot-motion cloud was shown centrally for up to 2.25 s. The motion direction was determined randomly in each trial (range: 1-360°). The target (i.e., a 30 ms saturation decrement) occurred at one of 26 possible times from 0.25 to 0.75 s relative to

stimulus onset. Participants were instructed to press the spacebar as fast as possible, once they detected the color change.

Quantification and statistical analysis

Analyses were performed with Matlab (The Mathworks Inc., Natick MA) using the FieldTrip toolbox [47]. We measured the accuracy for each target intensity at each temporal frame. Detection accuracy at the eight saturation levels for each frame were fitted with a cumulative normal Gaussian function using the Palamedes toolbox [48]. The function fit was performed with two free parameters (threshold and slope) and two fixed parameters (guess, set to zero, considering the exceedingly low chance level and lapse, set to 0.01). This experimental approach resulted in psychometric curves for each probed time point (Figure 1; the 26 possible time intervals). Figure S1 depicts the logic and the resulting psychometric curves for an example subject. All subsequent analyses of rhythmic fluctuations in behavior were performed on detection accuracy values at a fixed threshold intensity and on the 50% threshold estimates. The corresponding calculations are described below.

Analysis of behavioral fluctuations

Accuracy fluctuations

In the main accuracy analysis, we focused on a single intensity level out of eight. In order to select the relevant target-intensity, for each participant, we computed the average performance (hit rate) for each target-intensity level collapsing over all time bins. We then selected the target-intensity level (i.e., color-saturation decrement level) for which performance was closest to 50% accuracy for a given participant. We analyzed all the trials with that single, fixed, target level, and generated an accuracy time course. This analysis is similar to the analysis approach in previous studies investigating rhythmic sampling [7]. However, previous studies normally assessed the fixed intensity level in a separate "threshold block". A "threshold block" approach does not account for variability stemming from fluctuations over time, and thus such variability was treated as noise. We incorporated several intensity levels into the main experiment wherein time bins are exhaustively included by design. This enabled us to account for this variance and determine the intensity level for an accuracy analysis offline after, and based on, the collection of ongoing performance over time. For analysis of accuracy at a fixed target-intensity, individual subjects were included if the intensity level closest to 50% performance fell within the 25%-75% hit rate. In the two-cloud experiment the range of actual accuracy performance in this analysis was 28%-70% with a median of 60% for the blue cloud and 31.15%-72.3% with a mean of 50% for the red cloud. In the one-cloud experiment the range of accuracy was 37%-71% with a mean of 52%

performance. This criterion ensured that we measured performance with a sufficient dynamic range, avoiding performance at either ceiling or floor, which results in minimal or no dynamic range. This criterion resulted in the inclusion of 34 out of 36 and 22 out of 25 subjects for the one-cloud and two-cloud experiments, respectively. In order to quantify fluctuations in performance for each subject we de-trended the accuracy time course (2^{nd} order polynomial removal), windowed the data using a Tukey window [49], with a ratio of 50% taper section to total segment length. Data were then padded to double its sample count (52 samples) and subjected to a fast Fourier transform using the Fieldtrip toolbox in Matlab as well as built-in functions. Figure 3A, C depicts the average of individual subject spectra.

Threshold-estimate fluctuations

In addition to analyzing the accuracy-time course, which summarizes binomial performance, we sought to track continuous perceptual threshold fluctuations. To this end, we also analyzed the unfolding of detection threshold-estimates. For each time bin, after fitting accuracy data from each target-intensity with a psychometric curve (cumulative normal), we identified the target intensity that corresponded to 50% detection threshold for each time bin separately. We then constructed a time course from target-intensity (i.e., saturation decrement) values that corresponded to the threshold estimates (rather than accuracy values). In the one-cloud experiment, 3 subjects were excluded due to either an excessive guess rate or lapse (greater than 20% on either side, indicating that the target intensity range was not specified correctly for their level of performance), and 2 additional subjects were excluded due to poor fitting of psychometric curves (median pDev across time bins < .1; pDev is a measure of goodness of fit ranging between [0 1]). All subjects were included in the two-cloud experiment. The detection of a color saturation decrement could have a very broad range. In order to account for the fact that target intensity varied and thus global threshold estimates from different subjects came from different target intensity ranges, we normalized the threshold time-courses so that all participants' best performance value is 1, by dividing the time course values by maximal saturation values of the respective time course. This limited the upper bound of target intensity but allows different range of fluctuation depth in the data. The time-courses constructed from normalized threshold estimates were then subjected to a spectral analysis identical to that presented in the accuracy time course analysis (described above). Figure 4A, B depicts the results for this analysis approach.

Phase relation analysis

In the two-cloud experiment the phase relation was quantified for the significant peak frequency at 4 Hz. For this analysis the fast Fourier transform was performed on the time courses. Phase differences were then calculated based on the complex Fourier outputs for

4 Hz. Specifically, sampling of the items in alternation predicts phase opposition (180° phase difference). This analysis was performed for both accuracy performance measures and threshold performance measures, and depicted for accuracy performance in Figure 3B.

Analysis of eye-movement

We analyzed the eye-movement data of 28 and 19 subjects in the one- and two-cloud experiments, respectively. In the one-cloud experiment, out of the original 36 subjects, 6 were missing the raw data files from the eye tracker, 2 had extensive amounts of missing eye data due to calibration failures midway through the experiment, and 2 were recorded only monocular data due to calibration difficulties. These last two were included in the following analyses, but their microsaccade detection process was based on monocular data only. In the two-cloud experiment, out of the original 25 subjects, 2 were missing the raw data file from the eye tracker on one session and 4 subjects had missing data due to calibration difficulties midway through the experiment (1 subject on both sessions and 3 subjects on one).

We identified microsaccades as follows. Gaze position and pupil dilation data were recorded binocularly at 1000 Hz, and were epoched from cloud onset to target onset in the one-cloud experiment; and in the two-cloud experiment from the 1st cloud onset to the 2nd cloud onset (denoted here Phase I), and from the 2nd cloud onset to target onset (denoted Phase II; catch trials were excluded from all following analyses). Note that these epochs varied in length between 0.25-0.75s, depending on the time-bin in which the target appeared or the asynchrony of cloud appearance.

Preprocessing and microsaccade detection

We excluded from further analysis those epochs that included missing or deviant pupil data (z-score threshold set to -3, the mean and SD estimates used for z-thresholding were calculated over blocks of 20 experimental trials, excluding missing data points; these artifacts were padded by 100ms on either side to ensure gaze position data included no overshoot that might be falsely detected as a microsaccade). This exclusion criterion left all subjects whose data was originally included in the analysis of eye movements with above 30 and 60 trials per target onset condition in the one- and two-cloud experiments, respectively.

Gaze position data was subsequently demeaned and filtered using a low-pass Butterworth IIR filter with a cutoff of 60 Hz, and transformed from pixels degrees of visual angle. Saccades were detected following standard procedure [50] and using an established algorithm [51], in which vertical and horizontal gaze velocity is compared against an elliptic velocity threshold. The elliptic threshold was set to be six times the SD of the velocity time-series, using a median-based estimate of the SD. This threshold was calculated based on the entire velocity

time-series (combined across epochs) to protect detection from being biased by the variable trial length, and resulting in a single threshold criterion per subject. A saccade was identified when the velocity time-series exceeded the elliptic threshold for 6 consecutive samples, in both eyes (imposing a 6 ms minimal duration for detected saccades, and restricting the analysis to binocular saccades). Saccades with a peak velocity higher than 3 SDs from the mean (in either eye) were excluded from further analyses. We set the minimal interval between saccades to 50 ms, and kept the saccade larger in amplitude in case two saccades occurred during an interval of 50 ms or less. Saccade amplitude was calculated as the Euclidean distance between the most eccentric to the least eccentric position of gaze during the saccade, averaged between the two eyes. We restrict the following discussion to saccades smaller than 2 degrees of visual angle in amplitude, henceforth referred to as microsaccades.

As a validity measure of the detected microsaccades, we ensured that they followed the expected correlation between microssacade velocity and amplitude. The Pearson coefficient r was >0.83 for all participants.

Microsaccade direction was calculated as the four-quadrant inverse tangent of the vertical and horizontal microsaccade components (the vertical and horizontal difference in gaze position between the first and last microsaccade samples, averaged between the two eyes). Our eye-tracking device is set such that the coordinates to the top-left corner of the screen are set to (0,0), and therefore growing values on the vertical axis correspond to lower positions on the display. We thus inverted the sign of the vertical component in the calculation of microsaccade direction to maintain an upright axis.

Performance in microsaccade-free data

We repeated the analysis of accuracy fluctuations (see above) considering only the subset of trials that were free of microsaccades. Thus, we analyzed the remaining trials of 16 subjects in the two-cloud experiment (excluding the three subjects with insufficient dynamic range from the group of 19) and 26 subjects in the one-cloud experiment (excluding the two subjects with insufficient dynamic range from the group of 28), using each subject's selected target-intensity level for which performance was closest to 50% accuracy. The average (and SD) proportion of trials that were submitted to this analysis was 0.68 (0.01) and 0.53 (0.2) in the two- and one- cloud experiments, respectively. Due to the subsampling, in the calculation of accuracy time courses, 2% and 8% of the timepoints were missing in the two- and one- cloud experiments. In these cases, we imputed missing points with individual subject means.

Directional selectivity of microsaccades

We examined the possibility that our stimuli induce directional microsaccades consistent with the dot-motion direction. Trials from the two-cloud experiment were included in this analysis. Since trials contain 0.25-0.73 s of a single cloud presentation before the onset of the second cloud, this allows for a within-subject examination of microsaccade directionality both when viewing one cloud and when the second cloud is added to the display. On each trial that included a microsaccade, we subtracted the direction of the first cloud motion from the direction of the executed microsaccade on that trial. This results in a distribution of microsaccade directions that share a single angle axis per subject, a distribution that can be investigated as a function of the microsaccade time during the trial. An experimental trial was generally divided into two different phases based on the amount of clouds and motion displayed. Phase 1 is the epoch in which the first cloud is displayed. Phase 2 is the epoch in which a second cloud is added to the display and thus two clouds are simultaneously on, moving coherently in two different directions (always separated by 90°). These results are depicted in Figure S3.

Statistical Analysis

Accuracy fluctuations

Statistical significance of the spectral-amplitude peaks was assessed using a randomization procedure. The null hypothesis states that there is no temporal structure in performance. We used the response variation intrinsic to our data to generate performance time courses devoid of temporal structure. Per subject, we performed one thousand random exchanges within each time bin across all intensity levels. On each iteration we selected the target-intensity level for which the proportion of hits was closest to 50%, we generated an accuracy time course of trials in that intensity level, and finally quantified the fluctuation of this accuracy time course in the exact same fashion as used for the observed accuracy fluctuations, averaging the resulting power spectra across subjects. Each iteration resulted in an average spectral amplitude at each frequency. However, a single randomization distribution was generated from this procedure by selecting, per iteration, the maximal amplitude value across frequencies generated from the shuffling procedure. This approach corrects for multiple comparisons over the different frequencies explored in these analyses [43].

Threshold-estimate fluctuations

Statistical significance of the spectral-amplitude peaks was assessed using a randomization procedure. The null hypothesis states that there is no temporal structure in performance, and therefore the time points are exchangeable. The null distribution of power estimates was obtained by randomly shuffling the time courses of intensity threshold estimates 1000 times within subject, thus dissociating performance from time bin, and computing the power spectra

of these permuted time courses using identical parameters. However, a single randomization distribution was generated from this procedure by selecting, per iteration, the maximal Fourier-amplitude value generated from the time-shuffling procedure, regardless of frequency. This approach corrects for multiple comparisons over the different frequencies explored in these analyses [43].

Phase relation analysis

For the phase analysis non-uniformity was tested using circular statistics on the phase difference values (Rayleigh test for non-uniformity in circular data, CircStats toolbox [52]).

Performance in microsaccade-free data

Statistical significance of the spectral-amplitude peaks was assessed using a randomization procedure. The null hypothesis states that there is no temporal structure in performance, and therefore the time points are exchangeable. The null distribution of power estimates was obtained by randomly shuffling behavioral responses 1000 times (within subject and within the saturation level used to compute the accuracy time course), thus dissociating performance from time bin, computing detection time courses over the permuted data and the power spectra thereof using identical parameters.

In the one-cloud experiment, the p-value at 8 Hz was obtained by considering the proportion of 8 Hz power estimates from a null distribution that were more extreme than the observed power estimate.

In the two-cloud experiment, the p-value at 4 were obtained by considering the proportion of 4 Hz power estimates from a null distribution that were more extreme than the observed power estimate for each target color.

Directional selectivity of microsaccades

We tested the difference in distributions of microsaccade directions as a function of the microsaccade time during the trial (Phase 1 or Phase 2, see section in the eye-data analysis above) using Kuipers test, a circular version of the Kolmogorov-Smirnov test of difference between the distribution of two samples, implemented in CircStats toolbox [52]).

Data and software availability

Behavioral data and raw eye-movement data will be made available upon request by contacting the Lead Contact, Ayelet N. Landau (ayelet.landau@gmail.com). Custom-built MATLAB scripts are available online: https://osf.io/jspdb/?view_only=15eb58ac0d904442bb4aa6ad574697dd.

KEY RESOURCES TABLE

The table highlights the genetically modified organisms and strains, cell lines, reagents, software, and source data **essential** to reproduce results presented in the manuscript. Depending on the nature of the study, this may include standard laboratory materials (i.e., food chow for metabolism studies), but the Table is **not** meant to be comprehensive list of all materials and resources used (e.g., essential chemicals such as SDS, sucrose, or standard culture media don't need to be listed in the Table). **Items in the Table must also be reported in the Method Details section within the context of their use.** The number of **primers and RNA sequences** that may be listed in the Table is restricted to no more than ten each. If there are more than ten primers or RNA sequences to report, please provide this information as a supplementary document and reference this file (e.g., See Table S1 for XX) in the Key Resources Table.

Please note that ALL references cited in the Key Resources Table must be included in the References list. Please report the information as follows:

- **REAGENT or RESOURCE:** Provide full descriptive name of the item so that it can be identified and linked with its description in the manuscript (e.g., provide version number for software, host source for antibody, strain name). In the Experimental Models section, please include all models used in the paper and describe each line/strain as: model organism: name used for strain/line in paper: genotype. (i.e., Mouse: $OXTR^{fl/fl}$: B6.129(SJL)-$Oxtr^{tm1.1Wsy/J}$). In the Biological Samples section, please list all samples obtained from commercial sources or biological repositories. Please note that software mentioned in the Methods Details or Data and Software Availability section needs to be also included in the table. See the sample Table at the end of this document for examples of how to report reagents.

- **SOURCE:** Report the company, manufacturer, or individual that provided the item or where the item can obtained (e.g., stock center or repository). For materials distributed by Addgene, please cite the article describing the plasmid and include "Addgene" as part of the identifier. If an item is from another lab, please include the name of the principal investigator and a citation if it has been previously published. If the material is being reported for the first time in the current paper, please indicate as "this paper." For software, please provide the company name if it is commercially available or cite the paper in which it has been initially described.

- **IDENTIFIER:** Include catalog numbers (entered in the column as "Cat#" followed by the number, e.g., Cat#3879S). Where available, please include unique entities such as RRIDs, Model Organism Database numbers, accession numbers, and PDB or CAS IDs. For antibodies, if applicable and available, please also include the lot number or clone identity. For software or data resources, please include the URL where the resource can be downloaded. Please ensure accuracy of the identifiers, as they are essential for generation of hyperlinks to external sources when available. Please see the Elsevier list of Data Repositories with automated bidirectional linking for details. When listing more than one identifier for the same item, use semicolons to separate them (e.g. Cat#3879S; RRID: AB_2255011). If an identifier is not available, please enter "N/A" in the column.
    - ***A NOTE ABOUT RRIDs:*** We highly recommend using RRIDs as the identifier (in particular for antibodies and organisms, but also for software tools and databases). For more details on how to obtain or generate an RRID for existing or newly generated resources, please visit the RII or search for RRIDs.

Please use the empty table that follows to organize the information in the sections defined by the subheading, skipping sections not relevant to your study. Please do not add subheadings. To add a row, place the cursor at the end of the row above where you would like to add the row, just outside the right border of the table. Then press the ENTER key to add the row. Please delete empty rows. Each entry must be on a separate row; do not list multiple items in a single table cell. Please see the sample table at the end of this document for examples of how reagents should be cited.

TABLE FOR AUTHOR TO COMPLETE

Please upload the completed table as a separate document. ***Please do not add subheadings to the Key Resources Table.*** *If you wish to make an entry that does not fall into one of the subheadings below, please contact your handling editor. (****NOTE:*** *For authors publishing in Current Biology, please note that references within the KRT should be in numbered style, rather than Harvard.)*

KEY RESOURCES TABLE

REAGENT or RESOURCE	SOURCE	IDENTIFIER
Antibodies		
Bacterial and Virus Strains		
Biological Samples		
Chemicals, Peptides, and Recombinant Proteins		
Critical Commercial Assays		
Deposited Data		
Experimental Models: Cell Lines		
Experimental Models: Organisms/Strains		
Oligonucleotides		
Recombinant DNA		
Software and Algorithms		
MATLAB 2016b, 2017a	The MathWorks Inc.	https://www.mathworks.com/
Custom-built MATLAB code	This paper	https://osf.io/jspdb/?view_only=6788d0719e024c59a2ebfecb897ccd87
PsychoPy2 toolbox	[46]	DOI: 10.1016/j.jneumeth.2006.11.017
Fieldtrip toolbox	[47]	http://www.fieldtriptoolbox.org/
Palamedes toolbox	[48]	http://www.palamedestoolbox.org/
CircStats toolbox	[52]	DOI: 10.18637/jss.v031.i10
Other		

Figure 1

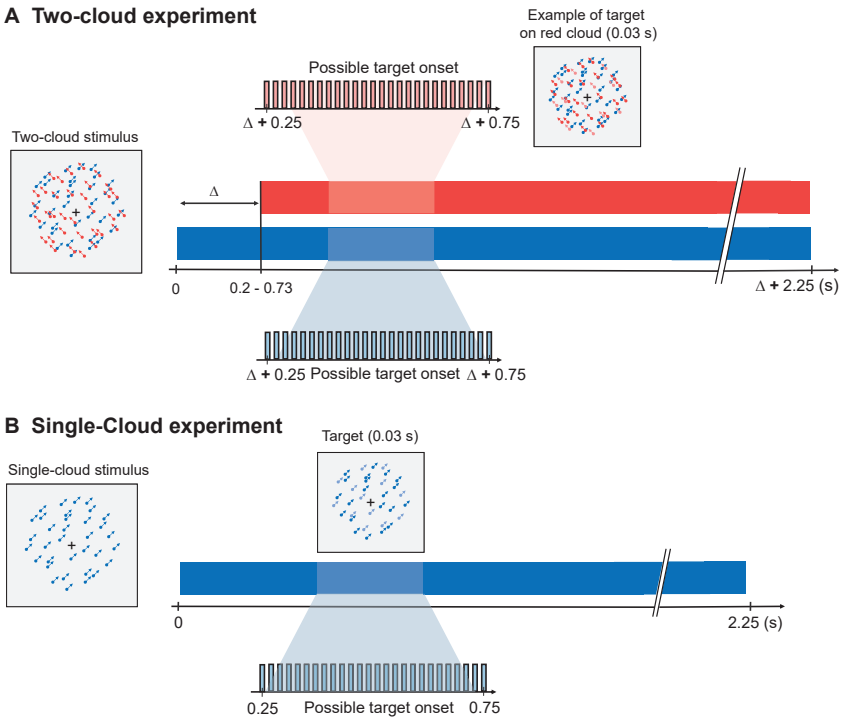
A Two-cloud experiment
Example of target on red cloud (0.03 s)
Possible target onset
Δ + 0.25
Δ + 0.75
Two-cloud stimulus
Δ
0
0.2 - 0.73
Δ + 2.25 (s)
Δ + 0.25 Possible target onset Δ + 0.75
B Single-Cloud experiment
Target (0.03 s)
Single-cloud stimulus
0
2.25 (s)
0.25
Possible target onset
0.75

Figure 2

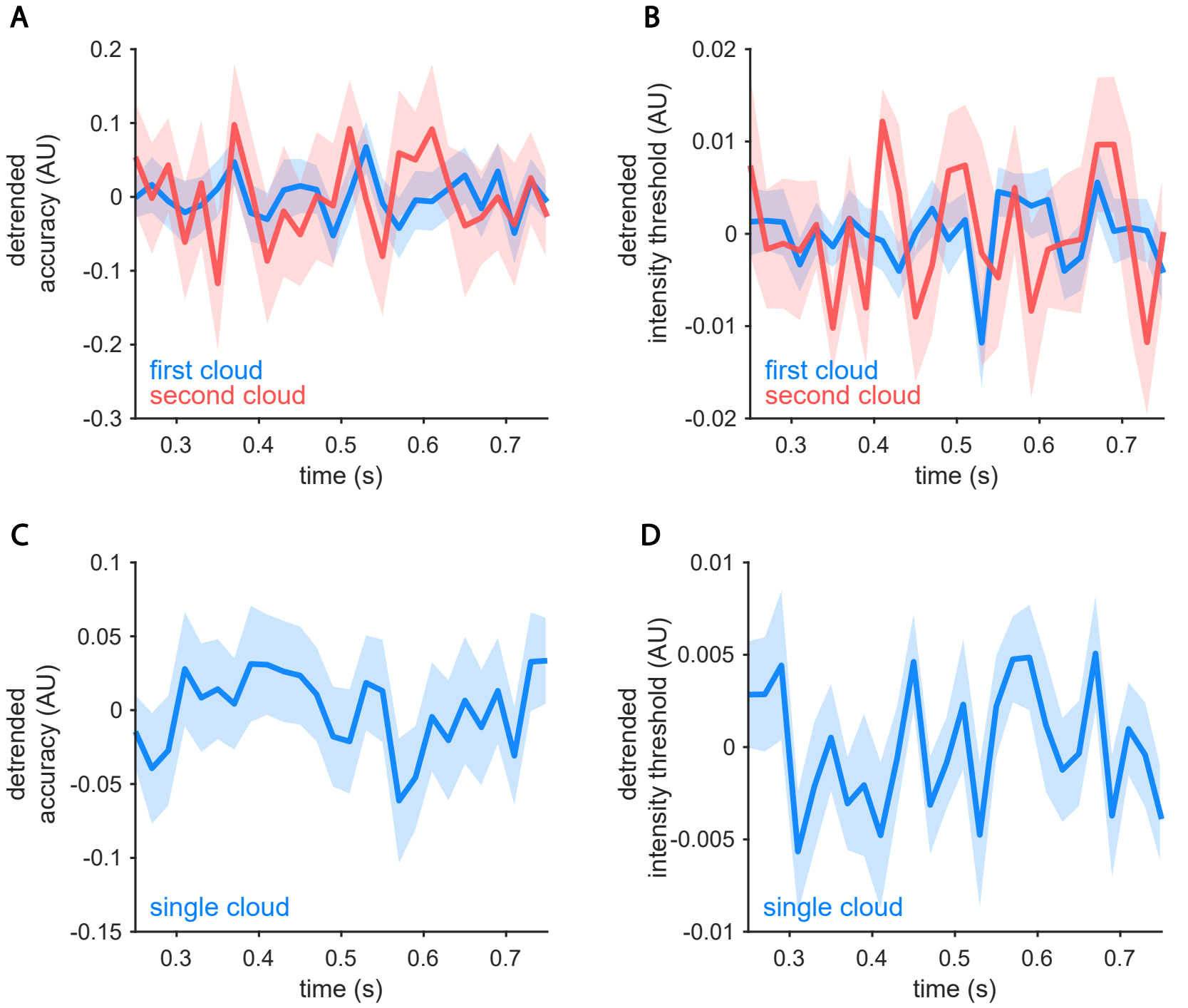
A
detrended accuracy (AU)
0.2
0.1
0
-0.1
-0.2
-0.3
first cloud
second cloud
0.3
0.4
0.5
0.6
0.7
time (s)
B
detrended intensity threshold (AU)
0.02
0.01
0
-0.01
-0.02
first cloud
second cloud
0.3
0.4
0.5
0.6
0.7
time (s)
C
detrended accuracy (AU)
0.1
0.05
0
-0.05
-0.1
-0.15
single cloud
0.3
0.4
0.5
0.6
0.7
time (s)
D
detrended intensity threshold (AU)
0.01
0.005
0
-0.005
-0.01
single cloud
0.3
0.4
0.5
0.6
0.7
time (s)

Figure 3

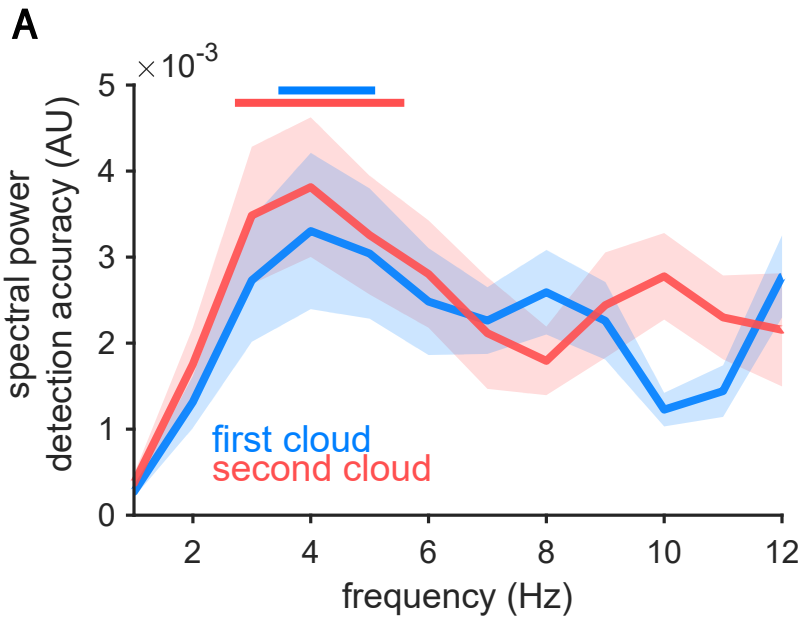
A
×10-3
5
4
3
2
1
0
spectral power
detection accuracy (AU)
first cloud
second cloud
2
4
6
8
10
12
frequency (Hz)

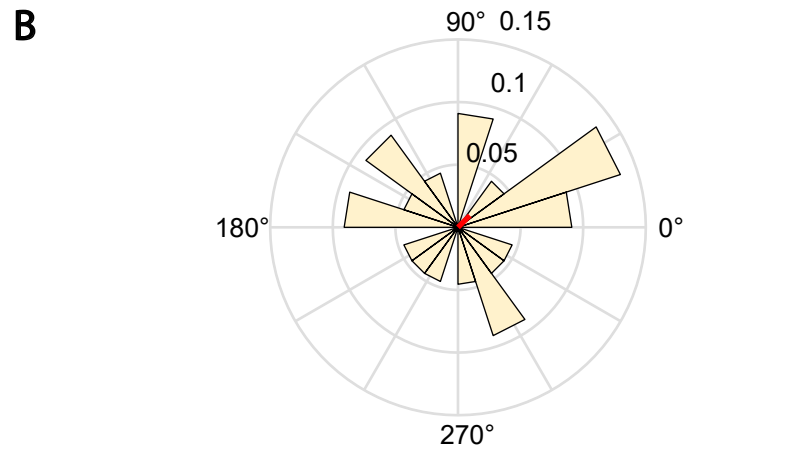
B
90°
0.15
0.1
0.05
180°
0°
270°

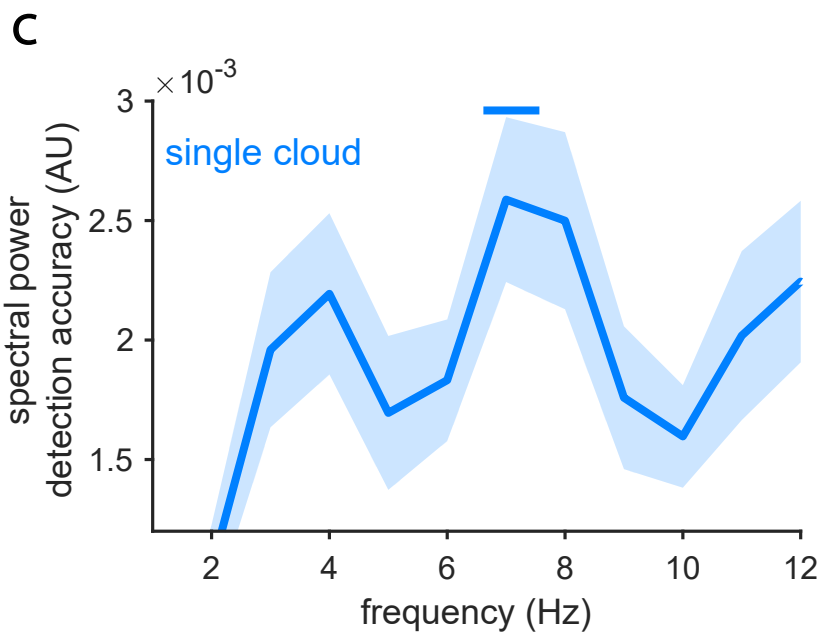
C
×10-3
3
2.5
2
1.5
spectral power
detection accuracy (AU)
single cloud
2
4
6
8
10
12
frequency (Hz)

Figure 4

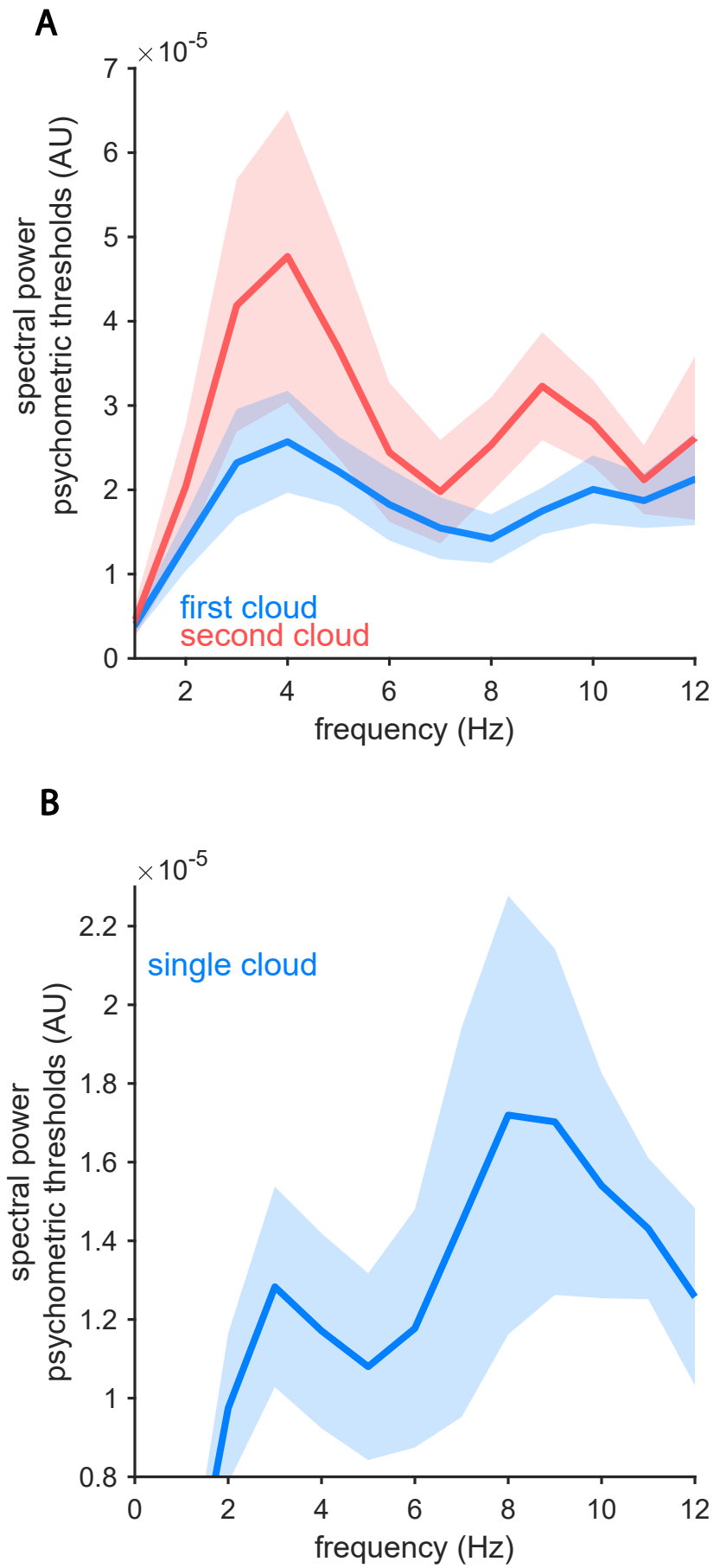
A
×10-5
7
6
5
4
3
2
1
0
spectral power
psychometric thresholds (AU)
first cloud
second cloud
2
4
6
8
10
12
frequency (Hz)
B
×10-5
2.2
2
1.8
1.6
1.4
1.2
1
0.8
single cloud
spectral power
psychometric thresholds (AU)
0
2
4
6
8
10
12
frequency (Hz)

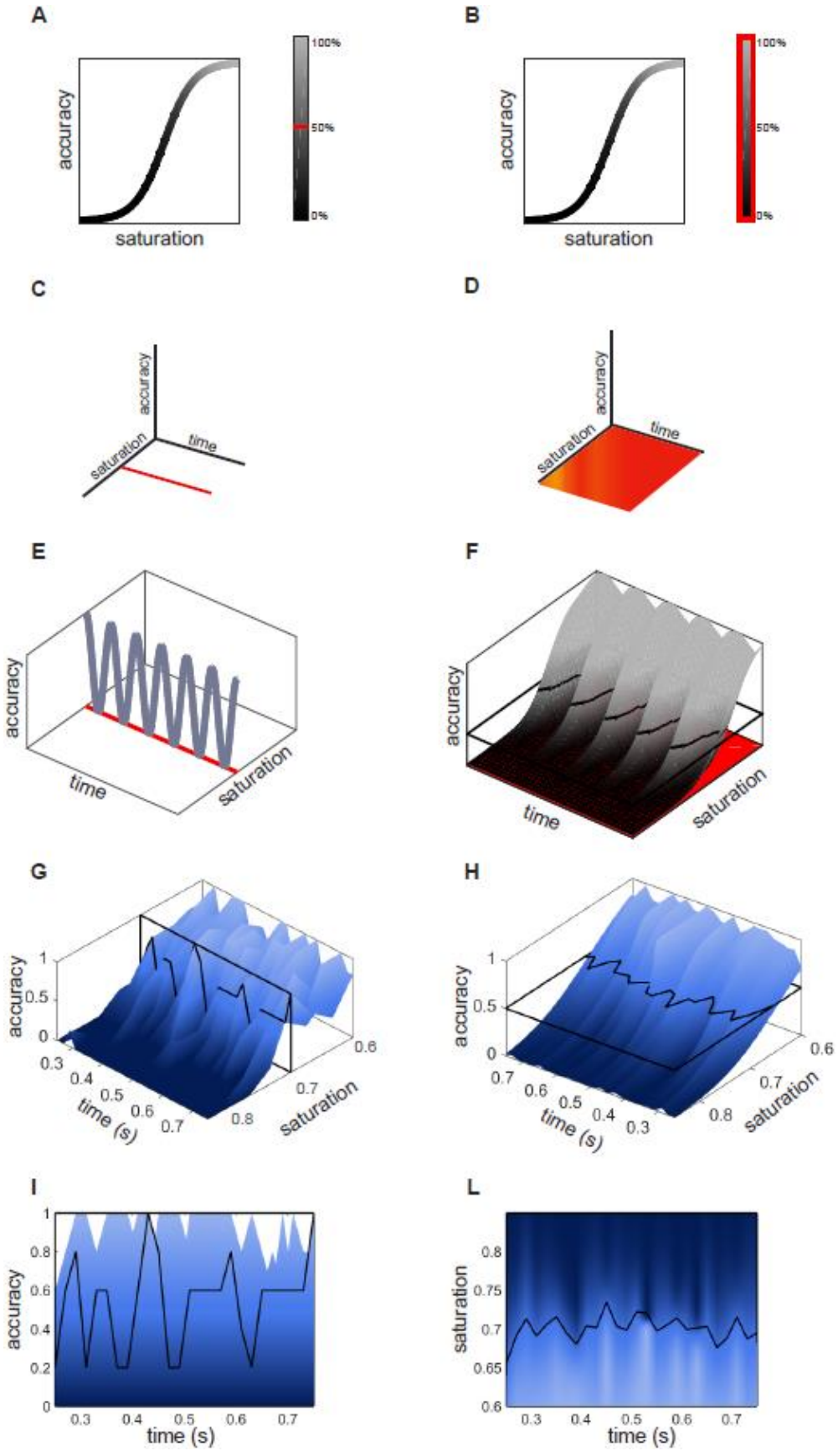
A
accuracy
saturation
100%
50%
0%
B
accuracy
saturation
100%
50%
0%
C
accuracy
saturation
time
D
accuracy
saturation
time
E
accuracy
time
saturation
F
accuracy
time
saturation
G
accuracy
1
0.5
0
0.3
0.4
0.5
0.6
0.7
0.8
time (s)
0.6
0.7
saturation
H
accuracy
1
0.5
0
0.7
0.6
0.5
0.4
0.3
time (s)
0.6
0.7
0.8
saturation
I
accuracy
1
0.8
0.6
0.4
0.2
0
0.3
0.4
0.5
0.6
0.7
time (s)
L
saturation
0.8
0.75
0.7
0.65
0.6
0.3
0.4
0.5
0.6
0.7
time (s)

Figure S1: Schematic illustration of the experimental approach and individual subject data for the single-cloud experiment. (A,C) Original reports of rhythmic sampling used a "threshold block" which assessed performance at different levels of target intensities (in this example, color-saturation, the x-axis of panel A). Then, derived from this block, the threshold level corresponding to 50% performance was identified (marked in red, at the 50% level) and used for the rest of the experiment. Panel C marks the parameter space that such an experimental block covers with a red line. (B,D) In the current design, all target intensities are used within the full experimental design. Thus, the full parameter space is included in the experimental design – as marked by the red surface in D. (E) illustrates the resultant hypothetical data from the original approach and (F) illustrates the hypothetical data from the current design where in each time point a function is fitted and the threshold is estimated. (G, H) demonstrate the individual subject data from the single-cloud experiment. (G) Raw data is plotted for all saturation levels over all time points. The data is not fitted by a psychometric curve, but the fixed target intensity level (i.e., saturation) is identified for which average performance is closest to 50%. At that fixed intensity, an accuracy time course can be composed from the different trials. (H) The same data as in G can be fitted with psychometric curves per time bin. Then, the threshold estimates from the function can be tracked as a function of time. (I) and (L) provide the two dimensional view of the measure of interest depicted in three dimensions in G and H. Color on blue surfaces denotes the accuracy level ranging from 0 (dark) to 1 (light-blue).

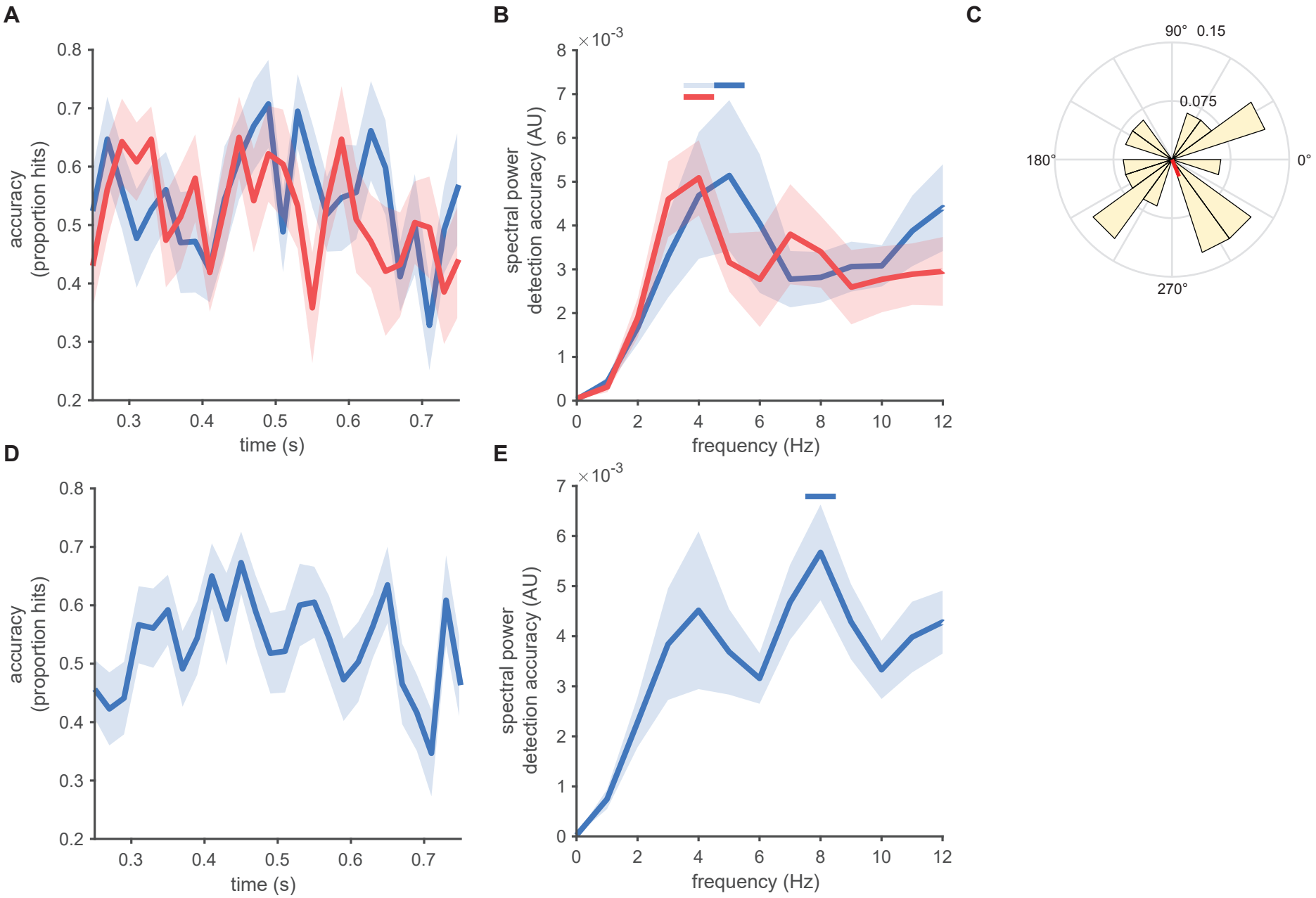
A
accuracy (proportion hits)
time (s)
B
spectral power detection accuracy (AU)
×10-3
frequency (Hz)
C
90° 0.15
0.075
180°
0°
270°
D
accuracy (proportion hits)
time (s)
E
spectral power detection accuracy (AU)
×10-3
frequency (Hz)

Figure S2: Time course of detection accuracy, and spectra for the two-cloud and one-cloud experiments, including only trials free of MSs. Note that time average data (A, D) only loosely represents the results reported here, since the main findings are generated from single-subject spectral analysis which is then entered into the statistical model or averaged for display purposes. Shaded regions denote ±SEM. (B) Amplitude spectra for the two-cloud experiment for accuracy measures. Blue and red lines represent first and second cloud stimuli. (C) Phase histogram for the phase relation between the first and second object performance at 4 Hz for accuracy measures. (E) Amplitude spectra for the single-cloud experiment for accuracy measures. Significance in all spectra, assessed for pre-determined frequency components ($p<0.05$), is denoted by a horizontal line above the significant frequency peaks; transparent horizontal line denotes a marginal effect ($p<0.07$). Shaded regions denote ±SEM.

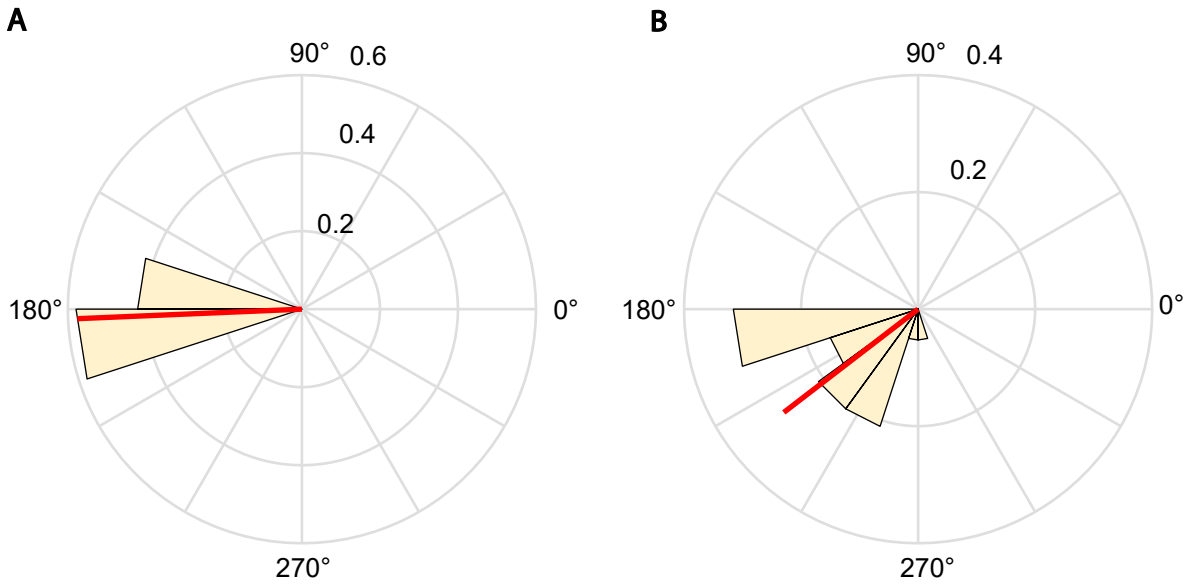

Figure S3: Directional selectivity of MSs. (A, B) Phase histograms for the subject mean directionality of MSs in the 2-cloud experiment during single-cloud presentation (i.e., during the interval Δ) and two-cloud presentation (i.e., after the onset of the second cloud), respectively. Direction 0 corresponds to the direction of movement of the first cloud dots.

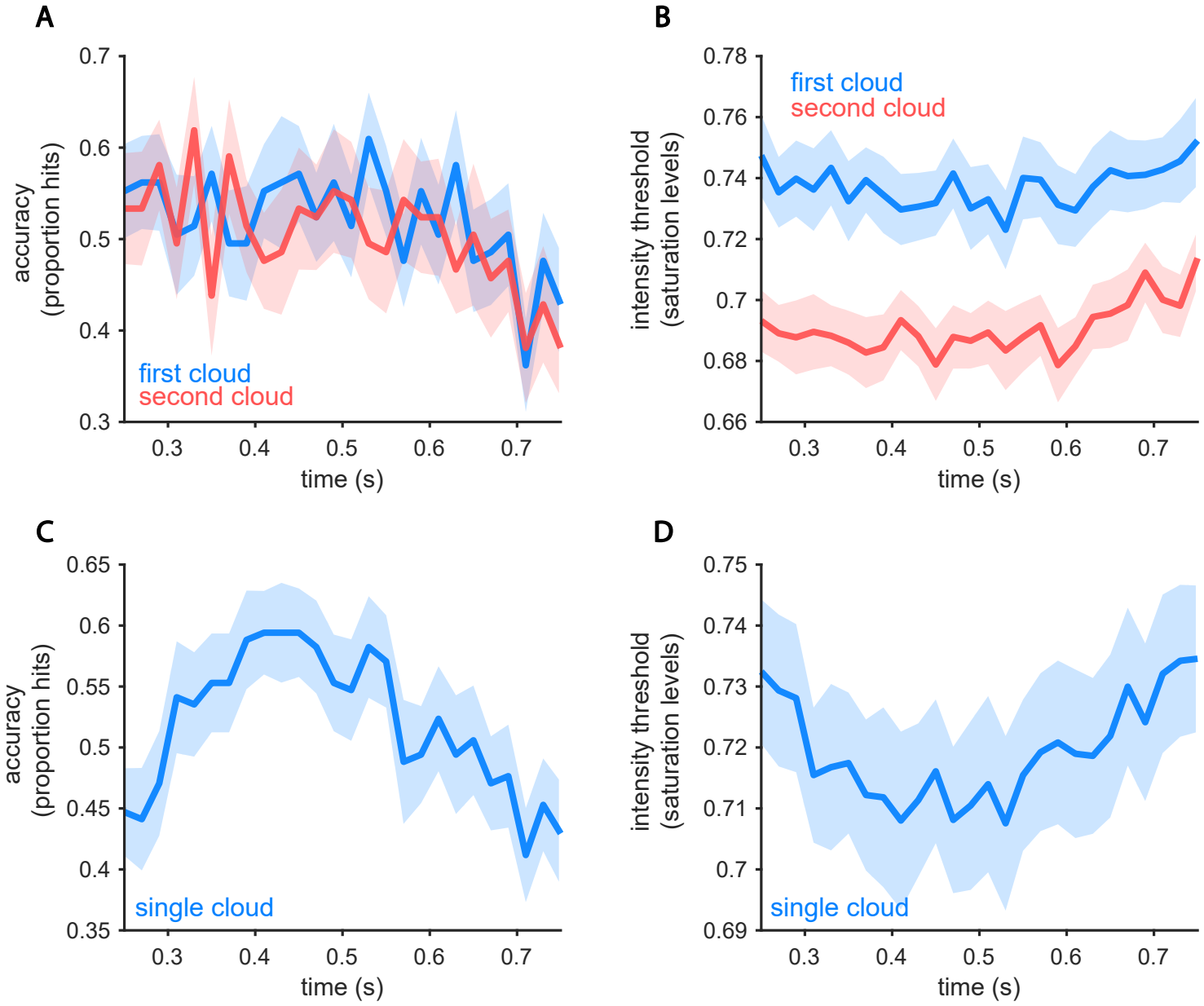

Figure S4: First and second experiment time courses for accuracy (A,C) and threshold (B,D). Raw average data identical to data presented in main Figure 2 except with no detrending applied.